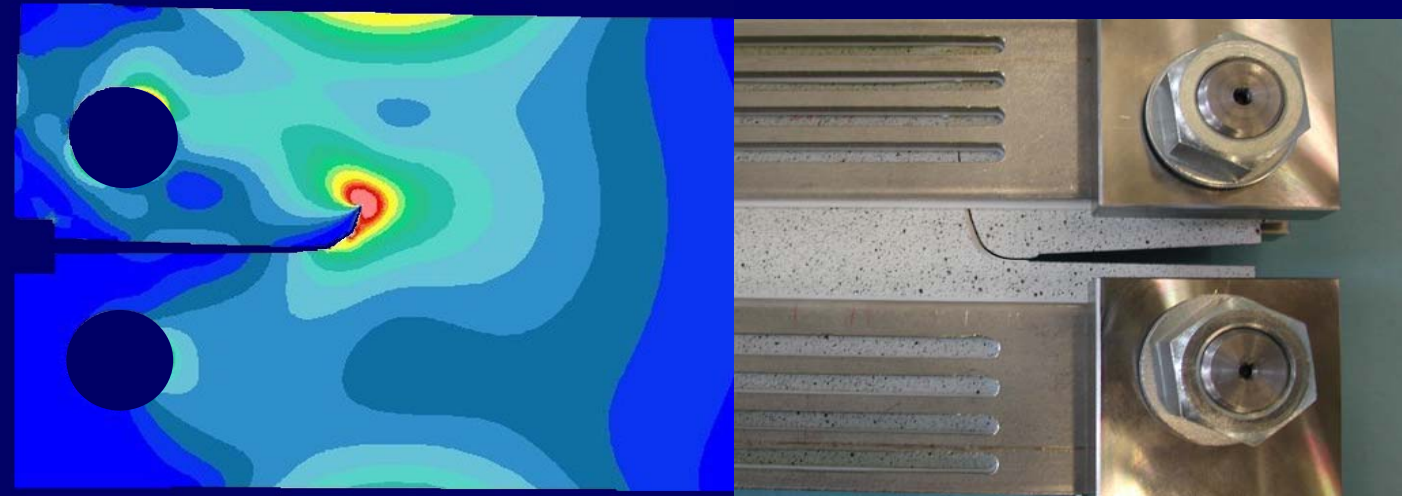


# Modelling and analysis of crack turning on aeronautical structures

Modelling and analysis of crack turning on aeronautical structures



*Doctoral Thesis*

*Llorenç Llopart Prieto*

*Director:*

*Dr. Marc Anglada i Gomila*



*Company director:*

*Elke Hombergsmeier*



Llorenç Llopart Prieto



*Ottoburnn / Barcelona April 2007*

*“Quia nolunt dimittere credere pro credere, sed credere per intelligere”*

**Ramón Llull, s. XIII**



## ***Abstract***

Developments in airplane structures are aimed at making them lighter, more durable, with higher damage tolerance and simultaneously safer than the existing riveted structures. Integral structures, monolithic or welded, offer weight reduction, costs savings and more corrosion resistance than differential structures (riveted). But, occasionally, they have lower tolerance to the damage. However, by testing these structures with cracks, it has been observed that crack turning may occur. This phenomenon produces an improvement of the damage tolerance inducing crack arresting or deflection.

In order to understand and assess crack turning in aeronautical structures, in this work it has been analysed different Finite Element (*FE*) tools capable to perform crack growth analyses on three dimensional models and, at the same time, with the ability to perform design studies. After assessing different *FE*-analysis tools, the commercial tool StressCheck<sup>®</sup> has been selected. The *T*-stress extraction facility has been implemented in StressCheck<sup>®</sup> in cooperation with Engineering Software Research & Development, Inc. The reliability of the tool has been proved to be satisfactory by means of literature and experimental test data. Using this tool and testing Double Cantilever Beam (*DCB*) as well as cruciform specimens under near in-plane opening mode (*Mode I*) loading conditions, different crack turning criteria have been checked.

Based on both testing and simulation results, a more developed criterion is proposed and some hints on the modelling process are recapitulated. The proposed criterion is based on existing criteria related to the *T*-stress and it is implemented with the normalised *T*-stress,  $T_R$ . The criterion takes into account the anisotropy of the material and the type of loading, i.e. quasi-static or cyclic loading. Its reliability is successfully proved by testing the *DCB*-specimens. The results of the work provide some confidence for using crack turning for the design process on airplane structures loaded under near *Mode I* conditions.

**Keywords:** Crack growth simulation; Crack turning; near *Mode I* loading; normalised *T*-stress; anisotropy; airplane structures.



# **Table of Contents**

<i>List of Figures</i>	i5
<i>List of Tables</i>	i11
<i>Nomenclature</i>	i13
<i>Abbreviations</i>	i17
<i>Acknowledgments</i>	i19
<b>1 Introduction</b>	<b>1</b>
<b>2 State of the art</b>	<b>5</b>
2.1 <i>Aeronautical structures</i>	5
2.1.1 <i>Aeronautical materials</i>	8
2.1.2 <i>Inspection intervals</i>	10
2.2 <i>Fracture Mechanics</i>	11
2.2.1 <i>Linear Elastic Fracture Mechanics</i>	12
2.2.2 <i>Elastic Plastic Fracture Mechanics</i>	15
2.2.3 <i>Plane strain and plane stress</i>	17
2.2.4 <i>The second order term and the two parameter characterisation</i>	18
2.2.5 <i>Fatigue</i>	21
2.3 <i>Numerical Methods</i>	24
2.3.1 <i>Crack growth simulation</i>	25
2.4 <i>Crack path</i>	27
2.4.1 <i>Rotation of the crack surface</i>	27
2.4.2 <i>Crack turning criteria for 2D-structures</i>	31
2.4.3 <i>Crack turning criteria for 3D-structures</i>	40
2.4.4 <i>Summary of crack turning criteria</i>	42
2.5 <i>Crack growth on fuselages</i>	42
2.5.1 <i>Load on aircraft structures</i>	44
2.5.2 <i>Crack turning on fuselages</i>	45
2.5.3 <i>The Doubler Cantilever Beam specimen</i>	48
2.5.4 <i>The cruciform specimen</i>	49
2.5.5 <i>Assessment of crack turning on the DCB-specimen</i>	50
<b>3 Objectives and Methodology</b>	<b>53</b>
3.1 <i>Modelling tool for crack growth analysis</i>	54
3.2 <i>Crack turning assessment</i>	55
<b>4 Experimental testing</b>	<b>57</b>
4.1 <i>Materials</i>	57

4.2	<i>Special characterisation techniques</i>	58
4.2.1	<i>The direct current potential drop method</i>	58
4.2.2	<i>Strain mapping system: ARAMIS<sup>®</sup></i>	59
4.3	<i>Experimental sets and results of testing</i>	60
4.3.1	<i>Standard tests</i>	60
4.3.2	<i>The Two-stringer specimen test (set reference DE03)</i>	67
4.3.3	<i>Crack turning specimens and tests</i>	70
<b>5</b>	<b><i>Modelling tool for crack growth analysis</i></b>	<b>83</b>
5.1	<i>Selection conditions</i>	83
5.2	<i>Modelling tools</i>	84
5.2.1	<i>NASGRO<sup>®</sup>/AFGROW<sup>®</sup></i>	84
5.2.2	<i>ANSYS<sup>®</sup></i>	85
5.2.3	<i>FRANC3D<sup>®</sup></i>	85
5.2.4	<i>Crack-Kit<sup>®</sup></i>	85
5.2.5	<i>StressCheck<sup>®</sup></i>	86
5.3	<i>Tested tools</i>	87
5.3.1	<i>First selection</i>	87
5.3.2	<i>Working with FRANC3D<sup>®</sup></i>	89
5.3.3	<i>Working with StressCheck<sup>®</sup></i>	94
5.3.4	<i>Conclusion of the tool analyses</i>	100
5.4	<i>Implementation of the tool</i>	100
5.5	<i>Reliability of the tool</i>	102
5.5.1	<i>Theoretical Stress Intensity Factor calculation</i>	103
5.5.2	<i>Simulation results</i>	104
<b>6</b>	<b><i>Crack turning assessment</i></b>	<b>107</b>
6.1	<i>Results from test-set reference RU04</i>	108
6.1.1	<i>COD-F-Crack length</i>	110
6.1.2	<i>Crack path prediction on DCB-specimens</i>	112
6.2	<i>Modelling influences on crack path predictions</i>	116
6.2.1	<i>3D-effects</i>	116
6.2.2	<i>Notch geometry and Modelling details</i>	121
6.2.3	<i>Explanation for the observed crack propagation behaviour</i>	134
6.3	<i>Results from test-set reference DE05</i>	134
6.3.1	<i>Direction of extrusion</i>	136
6.3.2	<i>COD-F-Crack length</i>	137
6.4	<i>Boundary conditions study</i>	140
6.5	<i>Global specimen plastification</i>	146
6.6	<i>Crack path predictions</i>	151

6.7	<i>Compilation of criteria and definitions</i>	156
<b>7</b>	<b><i>Summary and Conclusions</i></b>	167
7.1	<i>Confirmed observations</i>	168
7.2	<i>Conclusion</i>	169
7.3	<i>Future Work</i>	170
	<b><i>References</i></b>	171
	<i>Standards</i>	181
	<i>Internet Web sites</i>	182
<b>A</b>	<b><i>Annexes</i></b>	A1
A.1	<i>Numerical methods</i>	A1
A.2	<i>Crack turning criteria</i>	A3
	A.2.1 <i>Crack turning criteria for 2D-structures</i>	A3
	A.2.2 <i>Crack turning criteria for 3D-structures</i>	A6
A.3	<i>Experimental tests</i>	A8
A.4	<i>Other modelling tools</i>	A9
	<b><i>Curriculum Vitae</i></b>	A11





## List of Figures

Figure 2.1.	Fuselage structure assemblies [1]	6
Figure 2.2.	Typical fuselage loads	7
Figure 2.3.	a) Differential and b) integral structures [11]	8
Figure 2.4.	The three principal fracture mode loadings	12
Figure 2.5.	Cylindrical coordinate system and stress components at a three dimensional (3D) crack front [22]	13
Figure 2.6.	J-integral definition	15
Figure 2.7.	CTOD and CTOA definition	16
Figure 2.8.	$K_I$ - $K_{II}$ and $K_I$ - $K_{II}$ - $K_{III}$ diagrams for plane/surface mixed mode load with failure curve/surface and threshold curve/surface	16
Figure 2.9.	Variation of stress and strain along a 3D-crack front [31]	17
Figure 2.10.	Schematic representation of a) stress singularity zone and b) process zone, $\rho$ , plastic zone, $r_p$ , and K-field domain, $R_k$	18
Figure 2.11.	Idealized plot of SIF-range and crack growth rate for a metal at a given mean cyclic stress	22
Figure 2.12.	a) Turning angle $\varphi_c$ under plane mixed mode loading. b) Twist angle $\psi_c$ under overlay Mode I and Mode III loading [14]	28
Figure 2.13.	Asymmetric crack tip deformation due to tight hydrostatic stresses and shear strains [27]	29
Figure 2.14.	Transition to slant crack growth under a) static loading and b) cyclic loading [16]	30
Figure 2.15.	Fracture surface separation for a) plane strain and b) plane stress [61]	30
Figure 2.16.	Development of the observed stresses by Erdogan & Sih [62]	32
Figure 2.17.	Experimental and assessed crack path on a narrow body fuselage panel test after the MTS-criterion [9]	33
Figure 2.18.	Crack path turning parameters	34
Figure 2.19.	Experimental and assessed crack path on a narrow body fuselage panel test after the WEF-criterion [9]	36
Figure 2.20.	Schematic orthotropic crack growth resistance	39
Figure 2.21.	Experimental and assessed crack path on a narrow body fuselage panel test after the WEFO-criterion [9]	40
Figure 2.22.	Sign of the angle depending on $K_{II}$ , i.e. $\tau_{xy}$	42
Figure 2.23.	Failure of a) Comet transport jet aircraft from fatigue. b) Aloha Flight 243 in which the airplane lost a large section of its upper fuselage due to MSD	43
Figure 2.24.	Crack turning and flapping in Boeing 707 barrel-test [8]	45
Figure 2.25.	Schematic longitudinal crack in the Airbus A320 fuselage [24]	46
Figure 2.26.	Asymmetrical CT-specimen [53]	48
Figure 2.27.	Mostovoy specimen. Different crack turning paths due to different tapered angles, $\alpha_M$ [88]	48
Figure 2.28.	SDCB-specimen	49
Figure 2.29.	Stress flow on the CFS-specimen	50

Figure 2.30.	Crack path assessment using the WEFO-criterion on DCB-specimen in a) L-T and b) T-L direction [23]	51
Figure 3.1.	Fuselage zones and crack scenarios with turning potential [89]	53
Figure 3.2.	Schematic representation of the tasks involved in this work	54
Figure 4.1.	Schematic illustration of the current potential drop method	58
Figure 4.2.	a) Standard dog-bone specimens in L, 45° and LT directions, b) test set-up for the specimens in a)	61
Figure 4.3.	True stress-true strain curve for AA 6013-T3 L, 45° and LT directions	61
Figure 4.4.	Dimensions of the MT-specimen reference DE02	62
Figure 4.5.	MT test-rig reference DE02	63
Figure 4.6.	Crack growth rate for all MT-specimens with a thickness of 1.6 mm	64
Figure 4.7.	Crack growth rate for all MT-specimens with a thickness of 2.5 mm	64
Figure 4.8.	Residual strength test curves for L-T specimens	65
Figure 4.9.	Residual strength test curves for 45° direction	65
Figure 4.10.	Residual strength test curves for T-L specimens	66
Figure 4.11.	Dimensions of the two stringer specimen (2SP)	68
Figure 4.12.	Location and form of the dopplers on the specimen. The doppler dimensions are plotted in Figure A.6	69
Figure 4.13.	2SP test-rig (reference DE03)	69
Figure 4.14.	Crack growth versus crack length for the 2SP	69
Figure 4.15.	SEM images of the 2SP fractured surface at a) before the stringer and b) direct near the stringer	70
Figure 4.16.	Dimensions of the DCB-specimen	71
Figure 4.17.	Crack path results for a 40 mm notched DCB under quasi-static loading	72
Figure 4.18.	Crack path results for a 90 mm notched DCB under quasi-static loading	73
Figure 4.19.	Crack path results for a 140 mm notched DCB under quasi-static loading	73
Figure 4.20.	Crack path results for a 90 mm notched DCB under cyclic loading	74
Figure 4.21.	Applied load vs. COD results for the DCB with 40 mm notch and under quasi-static loading	74
Figure 4.22.	Applied load vs. COD results for the DCB with 90 mm notch and under quasi-static loading	75
Figure 4.23.	Applied load vs. COD results for the DCB with 140 mm notch and under quasi-static loading	75
Figure 4.24.	a) DCB-specimens corresponding to the set reference DE05 b) definition of the notch angle $\psi$	76
Figure 4.25.	Clamping device including cylinder bearing	77
Figure 4.26.	Test-rig for set reference DE05	78
Figure 4.27.	Crack path results for the DCB under cyclic loading (reference DE05)	78
Figure 4.28.	Crack path results for the DCB under quasi-static loading (reference DE05)	79
Figure 4.29.	ARAMIS analysis a) focused zone b) graphical representation of the output data. (data worked with Matlab®)	79

Figure 4.30.	ARAMIS strain analysis. Cyclic loading. DCB_F4540_1	80
Figure 4.31.	ARAMIS strain analysis. Quasi static loading. DCB_S040_hc03	80
Figure 4.32.	a) Dimensions and b) test-rig of the CFS-specimen (reference RU06)	81
Figure 4.33.	Results of testing for the CFS-specimen (reference RU06) under cyclic load conditions a) obtained crack path and b) a vs. N	82
Figure 5.1.	a) MT-geometry model after being treated with OSM, b) 2SP full-meshed model after automatic crack propagation, c) crack mesh after 16 steps of automatic propagation	90
Figure 5.2.	a) Application point (C) of the through crack, b) bilinear mapping of the crack and c) automatic re-meshing for the MT-specimen	91
Figure 5.3.	Extraction of the Paris constants from the crack growth rate results for the MT-specimens loaded with 100 and 180 MPa in L-T direction. Specimen thickness = 1.6 mm	92
Figure 5.4.	Illustration of the analysis line (here red) for the extraction of the fracture mechanics parameters. Every orange line defines a crack front. In this case there are 17 crack fronts	93
Figure 5.5.	Test and simulation of the MT-specimen with a thickness of 1.6 mm and an upper stress of a) 100 MPa and b) 180 MPa	93
Figure 5.6.	Crack propagation on the 2SP using the full model and the crack turning capability	94
Figure 5.7.	Mesh and boundary conditions for a) quarter MT-model and b) half 2SP-model with StressCheck	95
Figure 5.8.	Mesh and boundary conditions for the full 2SP-model without crack modelled with StressCheck	96
Figure 5.9.	Crack tip mesh illustrating the path-integral (hatched contour)	96
Figure 5.10.	Experimental test and simulation results for the MT-specimen with a thickness of 2.5 mm	97
Figure 5.11.	Models for the 2SP-specimen a) with the crack in the skin and b) in the outer flange	98
Figure 5.12.	Experimental test and simulation results for the half 2SP-specimen	99
Figure 5.13.	Contour integral near the crack tip [99]	102
Figure 5.14.	DCB-specimen dimensions [9]	102
Figure 5.15.	Boundary conditions and mesh from the simulated DCB-specimen	104
Figure 6.1.	Representative results of crack path under cyclic and quasi-static loading for an initial notch length of 90 mm	108
Figure 6.2.	Representative results of crack path under quasi-static loading for an initial notch length of 40, 90 and 140 mm in L-T and T-L	109
Figure 6.3.	DCB-model with 40 mm notch with the crack path from test results of reference RU04	110
Figure 6.4.	Selected crack path coordinates	111
Figure 6.5.	Test and simulation results of the DCB with a 40 mm notch. F-COD-a relation	112
Figure 6.6.	Crack paths for the DCB-specimen in L-T direction with a notch length of 90 mm	113
Figure 6.7.	Crack path prediction results with a 2D-model with 40 mm notch under quasi-static loading	114
Figure 6.8.	Definition of the relative (Rel.) and absolute (Abs.) turning angle	115
Figure 6.9.	a) Fracture surface of the 2SP-specimen and b) 2SP-model with the crack front on a)	116
Figure 6.10.	Simulation results with straight crack front and curved crack front model [82]	117

Figure 6.11.	Modelled 3D crack fronts	118
Figure 6.12.	Definition of the locations at the crack front, where the fracture parameters were calculated	120
Figure 6.13.	Crack paths predicted for different crack fronts and analysed points	121
Figure 6.14.	DCB-solid model and sets definition	122
Figure 6.15.	Crack tip geometries and pre-crack positions	123
Figure 6.16.	Simplified CFS-models	123
Figure 6.17.	Full CFS-models without grooves	124
Figure 6.18.	Full CFS-models with grooves	124
Figure 6.19.	Automatic crack path calculations from the model with the rounded notch	125
Figure 6.20.	Crack path results for different crack increments (quadratic notch model)	126
Figure 6.21.	Crack path results for different polynomial order (round notch model)	126
Figure 6.22.	Crack path predictions on DCB for different notch thicknesses (round notch model)	127
Figure 6.23.	Automatic crack path prediction for different notch geometries and pre-crack lengths with $h_c = 1 \text{ mm}$	127
Figure 6.24.	CFS-crack path predictions using model 1 until model 3b with a notch gap of 1 mm	128
Figure 6.25.	CFS-crack path predictions using model 3a until model 4 with a notch gap of 1 mm	128
Figure 6.26.	CFS-crack path predictions using model 2 and different notch gaps	129
Figure 6.27.	CFS-crack path predictions using model 3a and different notch gaps	129
Figure 6.28.	Manual mesh and boundary conditions of the CFS-model	130
Figure 6.29.	Modelled crack tip positions	131
Figure 6.30.	Stress intensity factor under Mode I for the crack situated on the middle of the notch (I. Middle crack)	131
Figure 6.31.	T-stress for the crack situated on the middle of the notch (I. Middle crack)	132
Figure 6.32.	a) Stress intensity factor under Mode I and b) T-stress for the crack situated on the side of the notch (II. Side crack)	132
Figure 6.33.	SIF under Mode II for the crack situated on the side of the notch (II. Side crack)	133
Figure 6.34.	Crack paths from the experimental results of testing ref. DE05 with different notch characteristics: $h_c = 1.5$ or $0.3 \text{ mm}$ , $\Psi = 0^\circ$ or $45^\circ$ and notch lengths: $a_0 = 43, 38$ or $33 \text{ mm}$	135
Figure 6.35.	Summary of Figures 4.30 and 4.31; Strain at the crack tip analysed by means of ARAMIS	136
Figure 6.36.	Cube representation of the delivered sheet 2024-T3 analysed by means of an optical microscope	137
Figure 6.37.	Force vs. COD records for the DCB-specimens tested under quasi-static loading	138
Figure 6.38.	Force vs. crack propagation for the specimens tested under quasi-static loading (test ref. DE05)	138
Figure 6.39.	Displacement restrictions applied on nodes or edges with partial and total fixation	142
Figure 6.40.	Displacement restrictions applied on nodes or edges with partial and total fixation (continuation)	144
Figure 6.41.	Boundary conditions in agreement with the deformations obtained on experimental tests ref. DE05	144
Figure 6.42.	100x amplified deformation and stress distribution for the model on Figure 6.41	145

Figure 6.43.	DCB-specimen deformation for a turned crack path during a) experimental test ref. DE05 and b) from the simulation results	145
Figure 6.44.	Stability of the solution varying either the crack length or the specimen width	146
Figure 6.45.	Visual degree of plasticity for two representative DCB-specimens. The illustration below (Static 40 L-T) corresponds to an applied force of 10 kN to illustrate the meaning of plastic collapse	149
Figure 6.46.	Crack path prediction by means of different crack turning criteria for the 40 mm notched DCB-specimen	153
Figure 6.47.	Crack path prediction using the WEFO-criterion on L-T and T-L direction	154
Figure 6.48.	Schematic orthotropic parameter dependence ( $\xi$ )	158
Figure 6.49.	DCB-crack path prediction using the proposed criterion for the 40 mm pre-notched specimen in L-T direction under cyclic loading	159
Figure 6.50.	DCB-crack path prediction using the proposed criterion for the 40 mm pre-notched specimen in L-T direction under quasi-static loading	160
Figure 6.51.	DCB-crack path prediction using the proposed criterion for the 40 mm pre-notched specimen in T-L direction under quasi-static loading	160
Figure 6.52.	DCB-crack path prediction using the proposed criterion for the 90 mm pre-notched crack specimen in T-L direction under cyclic loading	161
Figure 6.53.	DCB-crack path prediction using the proposed criterion for the 90 mm pre-notched specimen in L-T direction under cyclic loading	161
Figure 6.54.	DCB-crack path prediction using the proposed criterion for the 90 mm pre-notched specimen in T-L direction under quasi-static loading	162
Figure 6.55.	DCB-crack path prediction using the proposed criterion for the 90 mm pre-notched specimen in L-T direction under quasi-static loading	162
Figure 6.56.	DCB-crack path prediction using the proposed criterion for the 140 mm pre-notched specimen in T-L direction under quasi-static loading	163
Figure 6.57.	DCB-crack path prediction using the proposed criterion for the 140 mm pre-notched specimen in L-T direction under quasi-static loading	163
Figure 6.58.	Crack path prediction using the proposed criterion on the CFS-specimen in L-T direction under cyclic loading	164
Figure A.1.	Lagrange shape function a) linear and b) quadratic	A1
Figure A.2.	Cubic shape function a) Lagrange and b) Hermite	A1
Figure A.3.	Schemas showing a) the competition of MHS and MSS criterion b) the type of failure determined by $K_I/K_{II}$ versus the material ductility $\tau_c/\sigma_c$	A4
Figure A.4.	Crack turning angle as a function of the elastic mixed mode parameters for different hardening exponents $n$ [26]	A5
Figure A.5.	a) stable crack $\beta^* < 0$ ; $\gamma^* < 0$ ; b) re-stabilized crack $\beta^* > 0$ ; $\gamma^* < 0$ ; c) prediction of instability $\beta^* < 0$ ; $\gamma^* > 0$ d) unstable crack $\beta^* > 0$ ; $\gamma^* > 0$	A6
Figure A.6.	Doppler dimensions a) rear and b) front	A8



## List of tables

Table 2.1.	Chemical weight composition of the AA 7075-T6 sheet [S1]	8
Table 2.2.	Chemical composition of the AA 2024-T3 sheet [S2]	9
Table 2.3.	Types of aircraft inspection [1]	11
Table 2.4.	$r_c$ literature values	38
Table 2.5.	Frequency of failure mechanisms	43
Table 4.1.	Chemical composition of the AA 2024-T3 sheet [S2]	57
Table 4.2.	Chemical composition of the AA 6013-T6 [S4]	57
Table 4.3.	Mechanical properties of AA 6013-T3 profile	60
Table 4.4.	Fracture toughness of AA 6013-T3 profile	66
Table 4.5.	Mechanical properties of AA 2024-T3 sheet with a thickness between 0.25-3.25 mm	66
Table 4.6.	Test-matrix for set reference RU04	72
Table 4.7.	Test-matrix for set reference DE05	77
Table 4.8.	Test-matrix summary	82
Table 5.1.	Tool evaluation	89
Table 5.2.	Standard elastic isotropic material properties of the AA 6013-T3 in L-direction	91
Table 5.3.	Paris constants	92
Table 5.4.	Number of elements for the meshed models in FRANC3D <sup>®</sup>	93
Table 5.5.	Forman constants	97
Table 5.6.	Number of elements for the meshed models in StressCheck <sup>®</sup>	99
Table 5.7.	Comparison between StressCheck <sup>®</sup> and FRANC3D <sup>®</sup>	100
Table 5.8.	StressCheck results for the DCB-specimen with $a/w = 0.5$ ; $h/w = 0.2$	105
Table 5.9.	Computed values of $K_I$ , $T$ and $B$ for DCB-specimen	105
Table 5.10.	Theoretical Value of the SIF on the analysed DCB-geometry	106
Table 6.1.	Coordinates of the selected crack path to be analysed by means of simulation	111
Table 6.2.	Correlation between crack tip position, COD and force for the DCB with 40 mm notch	111
Table 6.3.	Crack path calculations with the WEF-criterion with $r_c = 3$ mm	115
Table 6.4.	Received crack path data for a notch length of 90 mm in L-T under cyclic loading. Ref. RU04	119
Table 6.5.	Example of the notes recorded from specimen DCB_S4540_II	139
Table 6.6.	Comparison of forces determined by experimental testing (ref. DE05) and simulation for different crack lengths	140
Table 6.7.	Fracture mechanics results for the boundary analysis on the DCB-specimen with a notch length of 140 mm	143
Table 6.8.	$\sigma_T$ and $K_v$ calculations for different points at the crack path for the specimen DCB_S4540 loaded under quasi-static loading	148
Table 6.9.	$L_{rp}$ calculations for the DCB_S4540 specimen	149



<i>Table 6.10.</i>	<i>L<sub>rv</sub> calculations for the DCB_S4540 specimen</i>	150
<i>Table 6.11.</i>	<i>Definition of the y-coordinate for the a<sub>i</sub> positions</i>	150
<i>Table 6.12.</i>	<i>Plastic Collapse and complete failure positions</i>	151
<i>Table 6.13.</i>	<i>T<sub>RC</sub>-values for quasi-static and cyclic load for both L-T and T-L directions</i>	158

## Nomenclature

$\alpha$	plane stress/strain constraint factor	[-]
$\alpha_0$	$= -2k_{II}/k_I$	[-]
$\alpha_1$	$= K_{Ic}/K_{IIc}$	[-]
$\alpha_2$	$= K_{Ic}/K_{IIIc}$	[-]
$\alpha_e$	$= K_I/K_{II}$	[-]
$\alpha_{eq}$	$= \tan^{-1}(K_I/K_{II})$	[-]
$\alpha_M$	tapered angles for the Mostovoy specimens	[°]
$\beta$	$= 2\sqrt{2} T/K_I$	[-]
$\beta_m$	$= \left( \bar{K}_m^{n_0} - 1 \right) / \left( \bar{K}_m^{n_0} + 1 \right)$	[-]
$\delta$	crack tip opening displacement	[mm]
$\delta_{il}$	Kronecker symbol, defined to be 1 when $i = l$ and 0 when $i \neq l$	[-]
$\Delta a$	crack growth increment	[mm]
$\Delta K$	SIF-amplitude	[MPa*m <sup>1/2</sup> ]
$\Delta K_0$	empirical constant for the determination of $\Delta K_{th}$	[MPa*m <sup>1/2</sup> ]
$\Delta K_c$	$= K_c (1-R)$	[MPa*m <sup>1/2</sup> ]
$\Delta K_i$	SIF amplitude under Mode $i$ with $i = I, II$ or $III$	[MPa*m <sup>1/2</sup> ]
$\Delta K_{th}$	SIF-amplitude threshold	[MPa*m <sup>1/2</sup> ]
$\Delta K_{I,th}$	SIF-amplitude threshold for Mode $I$	[MPa*m <sup>1/2</sup> ]
$\Delta x$	crack increment on the $x$ -axis	[mm]
$\varepsilon_{ij}$	strain field at the crack tip with $i, j = x, y, z$	[%]
$\Gamma$	arbitrary contour around the crack tip	
$\varphi$	first cylindrical coordinate angle contained in the plane $xy$	[°]
$\varphi_c$	turning angle under plane mixed-Mode loading (Mode $I + II$ )	[°]
$\lambda$	$= \sigma_x/\sigma_y$ . Applied stress factor for the CFS-specimens	[-]
$\lambda(x)$	$y$ -component on the crack path corresponding to the $x$ -coordinate for a turned crack	[mm]
$\mu$	shear modulus of elasticity	[MPa]
$\nu$	Poisson's ratio	[-]
$\nu'$	$= 1$ for plane stress $= (1-2\nu)^2$ for plane strain	[-]
$\rho$	process zone	[mm]
$\sigma_0$	maximal applied stress (two-stringer specimen)	[MPa]
$\sigma'_I$	special principal stress	[MPa]
$\sigma_I, \sigma_{II}, \sigma_{III}$	Principal stresses	[MPa]
$\sigma^\infty$	far field stress normal to the crack	[MPa]

$\sigma_c$	critical stress, which defines the unstable crack growth	[MPa]
$\sigma_e$	Von Mises effective stress	[MPa]
$\sigma_h$	hydrostatic stress = $(\sigma_I + \sigma_{II} + \sigma_{III})/3$	[MPa]
$\sigma_{ij}$	stress field at the crack tip. $i, j = x, y, z$ for Cartesian coordinates and $i, j = r, \varphi, \psi$ for cylindrical coordinates	[MPa]
$\sigma_{\varphi\varphi}(HRR)$	tangential stress on the <i>HRR</i> -field	[MPa]
$\sigma_{max}$	maximum applied stress	[MPa]
$\sigma_T$	= $T \cdot \sigma^\infty$	[MPa]
$\tau$	= $T/R_{p0.2}$	[-]
$\tau_c$	= $K_{IIc} / \sqrt{2\pi r_c}$	[-]
$\omega$	Twist applied force angle	[°]
$\psi$	second cylindrical coordinate angle contained in the plane $yz$	[°]
$\psi_c$	Twist crack turning angle under overlapped loading modes ( <i>Mode I + Mode III</i> )	[°]
$\xi$	Elliptical function for $\xi = K_c, R_m$ and $T_R$	
$A$	elongation at fracture	[%]
$A_{di}$	analysis database	
$A_k$	empirical constant on the calculation of the fracture toughness	
$B$	biaxial parameter	[-]
$B_1, B_2$ $B_3, B_4$	empirical constant for the SINH crack growth rate law	
$B_k$	empirical constant on the calculation of the fracture toughness	
$C'$	Forman-Newman-deKoning constant	
$C_f$	constant for the Forman crack growth rate law	
$C_p$	constant for the Paris crack growth rate law	
$CTOD_c$	critical <i>CTOD</i> which defines the transition between stable and unstable crack growth	[mm]
$E$	Young's modulus	[MPa]
$\tilde{E}$	= $E/(1-\nu^2)$ for plane strain = $E$ for plane stress	[MPa]
$E_{di}$	equilibrium database	
$F$	Force	[N]
$G$	shear Modulus	[MPa]
$G_e$	energy release rate	
$H$	local stress triaxiality	[MPa]
$J$	$J$ -integral = $\int_{\Gamma} \left( w dy - T_i \frac{\partial u_i}{\partial x} ds \right)$	
$J_c$	critical <i>J</i> -integral which defines the transition between stable and unstable crack growth	
$K_I$	<i>SIF</i> at the turned crack tip defined after Richard	[MPa*m <sup>1/2</sup> ]

$K_c$	under cyclic loading it represents the <i>SIF</i> at which the crack propagates at a given rate, for quasi-static loading it is the fracture toughness	[MPa*m <sup>1/2</sup> ]
$K_c(\varphi)$	fracture toughness dependent on the anisotropy of the material	[MPa*m <sup>1/2</sup> ]
$K_i$	<i>SIF</i> under <i>Mode i</i> loading with $i = I, II$ or <i>III</i>	[MPa*m <sup>1/2</sup> ]
$K_{ic}$	fracture toughness under <i>Mode i</i> loading with $i = I, II$ or <i>III</i>	[MPa*m <sup>1/2</sup> ]
$\overline{K}_m$	$= \frac{K_c(\varphi)_{\varphi=90^\circ}}{K_c(\varphi)_{\varphi=0^\circ}}$	[-]
$K_v$	comparative <i>SIF</i>	[MPa*m <sup>1/2</sup> ]
$K_{v,I,II}$	comparative <i>SIF</i> under <i>Mode I</i> and <i>Mode II</i>	[MPa*m <sup>1/2</sup> ]
$K_{v,I,II,III}$	comparative <i>SIF</i> under <i>Mode I</i> , <i>Mode II</i> and <i>Mode III</i>	[MPa*m <sup>1/2</sup> ]
$L_{rp}$	Elastic-plastic behaviour of the ligament	[-]
$L_{rv}$	plastic degree of the ligament	[-]
$M_{cf}$	middle point at the crack front	
$N$	lifetime	[cycles]
$N_i$	shape function	
$O(l)$	contribution of higher order terms on the stress field at the crack tip	[MPa]
$Q$	triaxiality parameter	
$R$	stress ratio	[-]
$R_1, R_2$ $R_3$ and $R_4$	Richard constants for the determination of crack turning angles	[°]
$R_c$	effect of crack closure under constant amplitude loading	
$R_{di}$	representational database	
$R_k$	K-field domain	[mm]
$R_m$	ultimate yield strength	[MPa]
$R_{p0.2}$	yield strength	[MPa]
$S$	energy density	
$T$	uniform non-singular stress, normal to the crack line and dependent on type of loading and specimen geometry	[MPa]
$T_i$	traction vector	
$T_R$	normalised <i>T</i> -stress (after Pook [16])	[MPa]
$T_{xz}, T_{zx}$	shear components on the second order term of the William's expansion series for a 3D crack	[MPa]
$T_{zz}$	<i>z</i> -component of the second order term in the William's expansion series for a 3D crack = $\nu T$	[MPa]
$U'$	variable field	
$U'_i$	Variable field on nodal or integral points	
$Wt\%$	weight %	[%]
$Z$	contraction at fracture	[%]
$a$	current crack length	[mm]
$a_0$	initial crack length	[mm]

$a_{11}, a_{12},$ $a_{22}$ and $a_{33}$	parameters defining the energy density ( $S$ )	
$c_0$	intrinsic crack length = 0.102 mm	[mm]
$d$	fatigue crack length	[mm]
$da/dN$	crack growth rate	[mm/cycles]
$erfc$	complementary error factor	
$f, f^*$	body forces	[N]
$f_{ij}^I(\phi),$ $f_{ij}^{II}(\phi),$ $f_{ij}^{III}(\phi)$	functions dependent on crack length and geometry for <i>Mode I</i> , <i>Mode II</i> and <i>Mode III</i> respectively with $i, j = x, y, z$	
$f_F$	Forman-Newman-deKoning function	
$h$	specimen half height	[mm]
$h_c$	opening gap of the notch	[mm]
$k_i$	<i>SIF</i> on the crack path before turning under <i>Mode i</i> for $i = I, II$ or <i>III</i>	[MPa*m <sup>1/2</sup> ]
$l_d$	distance between the crack tip and the <i>CTOD</i> measure point	[mm]
$n$	strain hardening exponent	
$n_f$	exponent constant for the Forman crack growth rate law	
$n_F$	unit vector normal to $\Gamma$	
$n_o$	exponent for orthotropic crack turning calculations	
$n_p$	exponent constant for the Paris crack growth rate law	
$p$	Forman-Newman-deKoning exponent	
$q$	Forman-Newman-deKoning exponent	
$r$	distance from the crack tip (cylindrical and Cartesian co-ordinates)	[mm]
$r_0$	explicit distance from the crack tip = $\frac{9}{128\pi} \left( \frac{K_I}{T} \right)^2$	[mm]
$r_c$	material specific distance from the crack tip	[mm]
$r_{cf}$	fatigue characteristic length	[mm]
$r_{ch}$	crack tip parameter	[mm]
$r_f$	radius of the fuselage	[mm]
$r_p$	radius of the Irwin plastic zone	[mm]
<b><i>r-value</i></b>	anisotropy ratio	[-]
$t$	thickness	[mm]
$t_i$	surface traction	[N]
$u_i$	displacement	[mm]
$w$	specimen width	[mm]
$w_s$	strain energy density	
$x$	cartesian coordinate. Global is defined parallel to the initial notch direction and local in the direction of actual crack propagation	
$y$	cartesian coordinate. Global is defined perpendicular to the initial notch direction and local perpendicular to the actual crack growth direction	
$z$	cartesian coordinate in the specimen thickness direction	

## ***Abbreviations***

<i>2D</i>	Two Dimensional
<i>2SP</i>	Two Stringer Specimen
<i>3D</i>	Three Dimensional
<i>A/C</i>	Aircraft
<i>AA</i>	Aluminium Alloy
<i>AIMS</i>	Airbus Industries Material Specification (Standard)
<i>BE</i>	Boundary Element
<i>BEM</i>	<i>BE</i> -Method
<i>CAD</i>	Computer Aided Design
<i>CATIA</i>	Computer-Graphics Aided Three Dimensional Interactive Applications
<i>CFS</i>	Cruciform Specimen
<i>COD</i>	Crack Opening Displacement
<i>Cr</i>	Chrome
<i>CRC</i>	Corporate Research Centre
<i>CT</i>	Compact Tension (Specimen)
<i>CTOA</i>	Crack Tip Opening Angle
<i>CTOD</i>	Crack Tip Opening Displacement
<i>CTS</i>	Compact Tension Shear (Specimen)
<i>DCB</i>	Double Cantilever Beam
<i>e<sup>-</sup></i>	Electron
<i>E&amp;Sih</i>	Erdogan & Sih (Criterion)
<i>EADS</i>	European Aeronautics Space and Defence (Company)
<i>EPFM</i>	Elastic Plastic Fracture Mechanics
<i>ESRD</i>	Engineering Software Research & Development (Inc.)
<i>Fe</i>	Iron
<i>FE</i>	Finite Element
<i>FEA</i>	<i>FE</i> -Analysis
<i>FEM</i>	<i>FE</i> -Method
<i>FNK</i>	Forman-Newman-deKonning
<i>HRR</i>	Hutchinson, Rice and Rosengreen (Field)
<i>IINT</i>	Interaction Integral (Method)
<i>LA</i>	Linear Analysis
<i>LEFM</i>	Linear Elastic Fracture Mechanics
<i>MAI</i>	Moscow State Aviation Institute
<i>Mg</i>	Magnesium
<i>MHS</i>	Maximum Hoop Stress (Criterion)
<i>MM</i>	Mixed Mode

<i>MMPDS</i>	Metallic Material Properties Development and Standardisation
<i>Mn</i>	Manganese
<i>Mode I</i>	In-plane opening mode
<i>Mode II</i>	In-plane sliding mode
<i>Mode III</i>	Out-of-plane tearing mode
<i>MPS</i>	Maximal Principal Stress (Criterion)
<i>MSD</i>	Multi Site Damage
<i>MSS</i>	Maximum Shear Stress (Criterion)
<i>MT</i>	Middle Cracked Tension (Specimen)
<i>NASA</i>	National Aeronautics and Space Administration
<i>NLA</i>	Non Linear Analysis
<i>OSM</i>	Object Solid Modeller
<i>R.T.</i>	Room Temperature
<i>SDCB</i>	Twist double cantilever beam
<i>SED</i>	Strain Energy Density
<i>SEM</i>	Scanning Electron Microscope
<i>Si</i>	Silicon
<i>SIF</i>	Stress Intensity Factor
<i>SwRI</i>	Southwest Research Institute
<i>TsAGI</i>	Central Aerodynamic Institute
<i>UPC</i>	Technical University of Catalonia
<i>UTC</i>	University of Technology of Compiegne
<i>VCCI</i>	Virtual Crack Closure Integral (Method)
<i>WEF</i>	Finnie & Saith, Kosai, Kobayashi & Ramulu and Shimamoto et al. (Criterion)
<i>WEFO</i>	<i>WEF</i> combined with fracture anisotropy (Criterion)
<i>Zn</i>	Zinc
<i>Zr</i>	Zircon

## ***Acknowledgments***

The investigation presented in this Ph.D. thesis has been possible with the support of many people. I would like to mention and thank them.

I would like to thank specially my wife Aline Licht for her patience and her predisposition to sacrifice weekends for letting me to work hard on the thesis during all these years.

I thank my family: Llorenç Llopart Domingo, Montserrat Prieto Seva and Roger Llopart Prieto and friend Dr. Lluís Gimeno Fabra for insisting and keeping faith in the outcome of my work.

I am also grateful to my thesis advisors Prof. Marc Anglada i Gomila and Elke Hombergsmeier and I would like to thank them for their efforts to monitor the technical contents and supervise the management activities. Special thanks to Aline, Lluís, Prof. Anglada, Joseph Barnett, Ignacio Morera Pintos and Dr. Claudio Dalle Donne during the process of writing of this thesis.

Particular thanks to my EADS colleagues with whom I shared impressions and opinions: Bernhard Kurz and Vitus Holzinger among others.

I express my gratitude to the staff of the Technical University of Catalonia (*UPC*), for their flexibility and understanding and to the friends there for their help in the bureaucracy: Dr. Jéssica Calvo Muñoz and Montserrat Charles-Harris Ferrer.

Finally, I would like to thank Dr. Herwig Assler and Dr. Alexei Vichniakov from Airbus for their cooperation and contributions on fatigue and damage tolerance applied in airplane structures.



